doi:10.14311/ppt.2026.2.49
Plasma Physics and Technology **13**(2):49–55, 2026

PLASMA-ASSISTED METHANE PYROLYSIS IN A DC THERMAL PLASMA TORCH: EXPERIMENTAL INVESTIGATION AND THERMODYNAMIC–KINETIC MODELING

A. Essiptchouk[a,*], F. Miranda[b], E. Prado[b], D. Leite[b], R. Segantine[b], G. Petraconi[b]

[a] *Department of Environment Engineering, Institute of Science and Technology, São Paulo State University, UNESP, São José dos Campos, 12245-000, Brazil*

[b] *Division of Fundamental Sciences, Technological Institute of Aeronautics, São José dos Campos,* ***12228-900*** *, Brazil*

[*] alexei.essiptchouk@gmail.com

Abstract. Methane pyrolysis in a DC nitrogen thermal plasma torch with post-discharge methane injection was investigated experimentally and numerically for low-carbon hydrogen production. Gas compositions were measured under steady operation and analyzed using thermodynamic equilibrium calculations and gas-phase kinetic modeling based on a reduced GRI-Mech 3.0 mechanism. High methane conversion and hydrogen fractions of 20–30 vol % were obtained. Kinetic results indicate that finite residence times and non-equilibrium effects explain the persistence of hydrocarbons, highlighting the advantages of post-discharge injection for stable plasma operation.

Keywords: Thermal plasma, Methane pyrolysis, Turquoise hydrogen, Plasma-assisted hydrogen production, Gas-phase kinetic modeling.

1. Introduction

The increasing urgency to mitigate climate change and reduce greenhouse gas emissions has driven the development of alternative energy pathways with lower environmental impact. Hydrogen has emerged as a strategic energy carrier for energy transition strategies, as its end-use does not involve direct carbon dioxide emissions [1]. However, the environmental performance of hydrogen strongly depends on the technological routes employed for its production, as well as on subsequent storage and distribution processes.

To distinguish these production pathways according to their environmental footprint, a color-based classification of hydrogen has been widely adopted. Gray hydrogen, primarily produced via steam methane reforming, is associated with significant CO_2 emissions. Blue hydrogen integrates carbon capture and storage technologies, yet remains dependent on fossil resources and exhibits uncertainties related to overall process efficiency. Green hydrogen, produced by water electrolysis powered by renewable energy sources, offers lower lifecycle emissions but is currently limited by high energy demand and production costs.

Turquoise hydrogen, obtained through methane pyrolysis, represents an alternative low-carbon pathway [2]. In this process, methane is thermally decomposed in the absence of oxygen to produce hydrogen and solid carbon, avoiding direct CO_2 formation. Key advantages of this route include higher energy efficiency compared to water electrolysis and the elimination of carbon capture requirements. The solid carbon by-product may be safely stored or valorized in industrial applications. Nevertheless, challenges remain regarding technological maturity, process scalability, operational costs, and effective management of the carbon phase.

Among the technologies associated with turquoise hydrogen production, thermal plasma-assisted methane pyrolysis has attracted increasing attention, including recent industrial-scale implementations. The high temperatures and energy densities characteristic of thermal plasmas promote efficient CH_4 dissociation, accelerated reaction kinetics, and high conversion levels [3, 4]. Experimental and theoretical studies have demonstrated the feasibility of this approach when powered by low-carbon electricity sources [5].

In addition to methane pyrolysis, other plasma-based routes for hydrogen production have been investigated, such as glycerol steam reforming and methanol decomposition in thermal plasma reactors. Reported results indicate high hydrogen yields, substantial carbon conversion, and competitive energy efficiencies, even in catalyst-free configurations [6–11]. These studies highlight the versatility of thermal plasma processes as platforms for low-carbon hydrogen production.

Despite these advantages, thermal plasma systems face several technical challenges, including high electrical energy consumption, equipment cost and complexity, arc instability, and carbon deposition on electrodes and internal torch components. To mitigate these issues, different methane feeding strategies have been

proposed. Direct injection of CH_4 into the electrical discharge region enhances plasma–reactant interaction but is often accompanied by ignition difficulties, arc instability, and rapid electrode carbonization. In contrast, methane injection into the plasma jet downstream of the discharge region enables prior plasma stabilization using auxiliary gases, reduces operational risks, and provides improved control over methane conversion and carbon morphology.

A comparative assessment of direct methane injection into the discharge zone and post-discharge injection into the plasma jet is therefore essential for elucidating the underlying physicochemical mechanisms and optimizing energy efficiency, operational stability, and product quality. Such analyses support the development of technically and economically viable thermal plasma-based routes for industrial-scale turquoise hydrogen production. Within this context, the present work focuses on the comparison between experimental measurements and thermodynamic–kinetic modeling predictions under representative operating conditions, rather than on reactor optimization or parametric performance evaluation.

2. Metodology

2.1. Experimental Setup

The experimental system is based on a direct current (DC) thermal plasma torch of the tornado type equipped with a hollow bottom cathode. The plasma torch was operated at a current of 150 A and an arc voltage of 250 V. The estimated thermal efficiency was 65 %, resulting in an effective plasma jet power of approximately 21 kW. A gas injector is installed at the torch outlet, enabling the introduction of the feed gas into the plasma jet in a special reforming chamber. Downstream of the reforming zone, a rapid cooling (quenching) system is employed to suppress secondary reactions and stabilize the reaction products.

Nitrogen was used as the plasma-forming gas at a flow rate of 90 standard liters per minute (slpm). Methane was injected into the plasma jet at a flow rate of 40 slpm. Additional nitrogen, supplied at 30 slpm downstream of the reforming chamber, was used to quench the products and rapidly reduce the gas temperature. All gas flow rates were controlled and monitored using mass flow controllers (MKS Instruments).

The outlet gas composition was analyzed both qualitatively and quantitatively using a portable gas analyzer (VARIOLUXX, Confor Instrumentos de Medição, in collaboration with MRU, Germany).

The injector geometry is shown in Fig. 1. A nitrogen plasma jet generated by the torch enters the injector axially, which has a diameter of 14 mm and a length of 70 mm. Methane, supplied at ambient temperature, is injected radially through three channels of 1.3 mm diameter into the plasma jet, with sufficient dynamic pressure to ensure penetration into the high-velocity plasma core. Downstream of the injection plane, the plasma-forming gas and the injected methane mix and interact along the flow direction.

A preliminary numerical simulation of the injector was performed under non-reacting flow conditions to assess the mixing characteristics of the system. The axial evolution and selected cross-sectional distributions of the methane volumetric fraction are presented in Figures 2 and 3. These distributions result from the interaction between the axial nitrogen jet and the radially injected methane stream. The values indicated in the figures correspond to the axial distance (in mm) from the injection plane.

The Figure 3 presents the cross-sectional distribution of the CH_4 volumetric fraction at different axial positions relative to the injection plane ($z = 0$ mm). At the inlet section, localized peaks of CH_4 concentration are observed near the radial injection points, indicating limited penetration into the axial N_2 flow and strong non-uniformity, with steep radial concentration gradients.

At $z = 10$ mm, the radial jets are deflected and stretched by the axial flow, leading to a redistribution of CH_4 into multiple regions of intermediate concentration. This behavior is characteristic of a convection-dominated regime, where a high Péclet number implies that advective transport prevails along the axial direction.

In the range $z = 20 - 30$ mm, a reduction in local concentration maxima is observed, accompanied by an increase in CH_4 concentration in regions that were initially depleted. This indicates enhanced mixing, with significantly reduced transverse gradients and an increasing contribution of diffusive mechanisms (molecular and/or turbulent, depending on the flow regime).

At $z = 40$ mm, the distribution becomes nearly uniform across the cross-section, with only minor residual spatial variations. This suggests that the local residence time is sufficient to promote advanced mixing between N_2 and CH_4, resulting in a smoothed concentration field approaching a homogeneous state.

2.2. Thermodynamic Model Description

The reactive chemical system is described using a thermodynamic equilibrium approach based on the minimization of the Gibbs free energy. This method enables the determination of the equilibrium composition without explicit specification of chemical reactions, requiring only the definition of the possible chemical species and their corresponding thermodynamic properties. The approach is particularly suitable for high-temperature systems in which chemical and phase transformations are assumed to reach local thermodynamic equilibrium.

The model accounts for both gaseous and condensed phases formed during the process. Thermodynamic properties and equilibrium compositions are calculated as functions of system temperature and pressure,

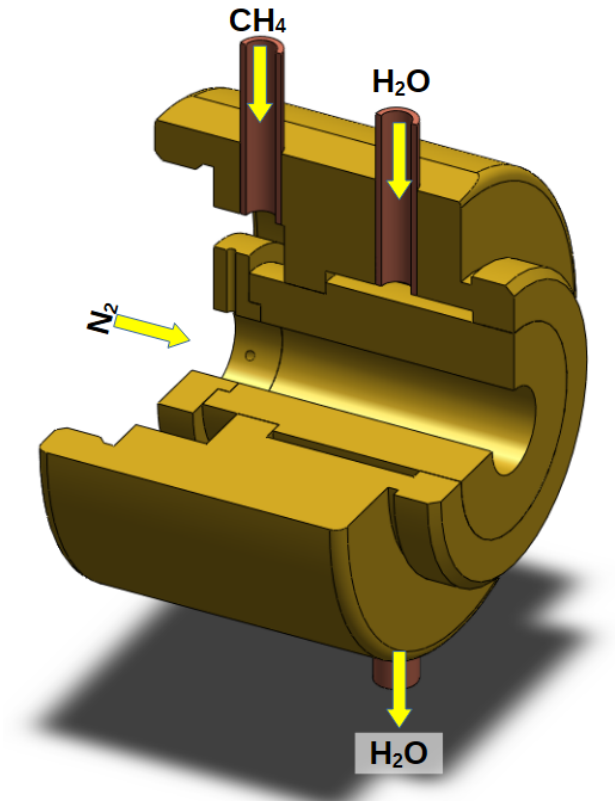

Figure 1. 3D schematic of the methane reforming device employed in the plasma reactor, indicating the N_2 and CH_4 inlets, together with the cooling water inlet and outlet, denoted as H_2O.

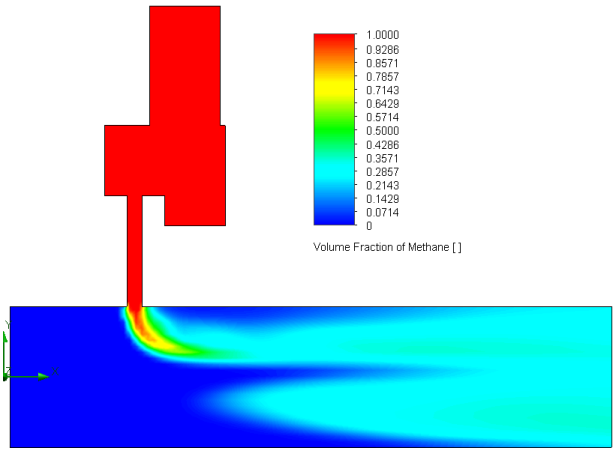

Figure 2. Axial evolution of the methane volumetric fraction along the reforming chamber.

considering the strong dependence of these properties on phase composition. Heat and mass transfer effects are implicitly reflected through the equilibrium formulation, which assumes a closed and isolated system under local thermal and chemical equilibrium conditions.

All calculations were implemented in the Python programming language using the Cantera open-source library, which provides robust tools for thermodynamic, kinetic, and transport modeling. The system was closed by specifying two independent state variables: temperature and pressure. The temperature was varied from 350 K to 5000 K, while the pressure was fixed at atmospheric conditions ($p = 0.1$ MPa). The chemical system included 65 species composed of carbon, hydrogen, and nitrogen.

2.3. Kinetic model description

The plasma-assisted chemical system is described using a kinetic approach that accounts for the temporal evolution of all reactive species involved in the process. The model is based on a detailed reaction mechanism composed of elementary reactions, each characterized by its corresponding rate coefficient.

Under homogeneous and zero-dimensional assumptions, the system is treated as spatially uniform, neglecting concentration gradients within the reactive volume. Although plasma-chemical processes typically occur under flowing conditions, this approach allows for the identification of dominant reaction pathways, characteristic reaction time scales, and kinetically limiting steps. Such simplifications are commonly adopted in plasma chemistry modeling when the objective is to analyze intrinsic chemical kinetics independently of transport effects.

To ensure consistency with strong variations in temperature, density, and total number of moles, the governing equations are formulated in terms of molar amounts n_i (mol) rather than concentrations. The temporal evolution of each species i is described by the following system of ordinary differential equations:

$$\frac{\mathrm{d}n_i}{\mathrm{d}t} = \sum_{r=1}^{N_r} \nu_{i,r} R_r \tag{1}$$

where N_r is the reactions number, $\nu_{i,r}$ is the stoichiometric coefficient of species i in reaction r, and R_r is the reaction rate of reaction r, given by mass-action kinetics:

$$R_r = k_r \prod_{j=1}^{N_s} \left(\frac{n_j}{V}\right)^{\nu_{j,r}} \tag{2}$$

Here, N_s is the number of species, k_r is the temperature-dependent rate coefficient expressed in Arrhenius form:

$$k_r = A_r T^{\beta_r} \exp\left(-\frac{E_{a,r}}{RT}\right) \tag{3}$$

where A_r, β_r , and $E_{a,r}$ are the pre-exponential factor, temperature exponent, and activation energy, respectively. The reactor volume V is not constant and is evaluated using the ideal gas law:

$$V = \frac{n_{\mathrm{tot}} RT}{P} \tag{4}$$

where $n_{\mathrm{tot}} = \sum_i n_i$ is the total number of moles. This formulation explicitly accounts for volume variations induced by changes in temperature and composition,

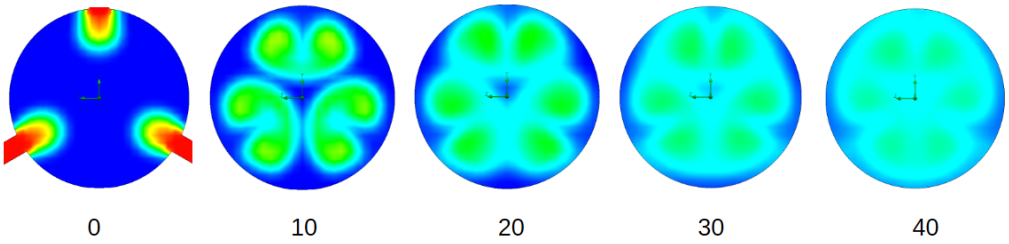

Figure 3. Cross-sectional distributions of the methane volumetric fraction at different axial distances from the injection plane.

which are particularly relevant in plasma-assisted systems.

The resulting system of coupled ordinary differential equations is highly stiff due to the wide range of reaction time scales and rate coefficients. Therefore, stiff numerical solvers with adaptive time-stepping are employed to ensure numerical stability and accuracy. Additional numerical constraints are applied to prevent nonphysical solutions, such as negative molar amounts.

In this study, methane pyrolysis is modeled using a detailed gas-phase kinetic mechanism involving 18 species H, H_2, CH_4, CH_3, CH_2, CH, C_2H_6, C_2H_5, C_2H_4, C_2H_3, C_2H_2, C_2H, C_4H_4, C_6H_6, nC_4H_5, C, C_2, and N_2, and 65 elementary reactions extracted from [5, 12].

This kinetic framework enables quantitative prediction of species evolution under strongly non-equilibrium conditions and provides a consistent basis for comparison with thermodynamic equilibrium calculations and experimental observations.

3. Results and discussion

Under steady-state operating conditions, the specific enthalpy of the nitrogen plasma jet was estimated as 11.24 $MJ\,kg^{-1}$, corresponding to an average plasma temperature of approximately 5965 K. While maintaining a constant nitrogen flow rate, methane was gradually introduced into the system, as illustrated in Figure 4. The same figure also reports the volumetric fractions of H_2 and CH_4 measured at the reactor outlet. It should be noted that the CH_4 analyzer measures the total hydrocarbon concentration, which is reported as methane-equivalent (CH_4-equivalent). During the stable operating interval between 9 and 15 min, the average methane flow rate was 40.2 slpm.

As a result of the interaction between methane and the nitrogen plasma jet, methane pyrolysis was activated, yielding an outlet gas composition containing 20.9 vol.% H_2 and 4.3 vol.% residual CH_4. The remaining gas fraction consisted predominantly of N_2, since nitrogen was employed both as the plasma-forming gas (90 slpm) and as the quenching gas (30 slpm), whereas the methane feed rate was limited to 30 slpm.

Under these conditions, the methane conversion was estimated to be approximately 92 %. The interaction between the methane flow and the plasma jet occurs

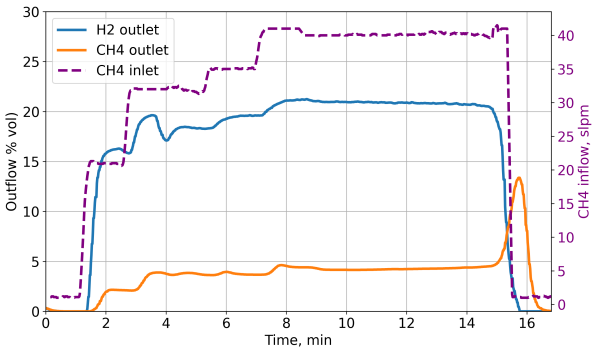

Figure 4. Time-resolved CH_4 feed rate and outlet concentrations of H_2 and CH_4.

under strongly turbulent conditions, promoting rapid mixing and thermal equilibration of the streams. At the outlet of the reforming chamber, the temperatures of the nitrogen plasma and methane streams are assumed to be equal.

Part of the thermal energy carried by the nitrogen plasma jet is transferred to the methane stream, providing the energy required for methane pyrolysis (Figure 5). For a continuous flow system, the thermal power associated with each stream can be expressed as $Q_i = H_i \dot{m}_i$ where H_i is the specific enthalpy and $\dot{m}_i$ is the corresponding mass flow rate, resulting in a heat flow expressed in watts.

Based on an enthalpy balance between the incoming N_2 plasma jet and the injected CH_4 stream, an effective mixing temperature of $T_{mix} = 2372$ K is obtained, assuming thermal equilibration between the two streams and neglecting chemical interactions between N_2 and CH_4. The resulting combined flow retains a total thermal power of approximately 7.7 kW.

It should be emphasized that this approach represents a global 0D energy estimate and constitutes a significant simplification of the actual plasma flow. In particular, it does not account for the strong axial and radial temperature gradients inherent to plasma jets, nor for non-equilibrium effects associated with finite-rate chemistry. The use of thermodynamic enthalpies implicitly assumes local thermodynamic equilibrium (LTE), which may not be strictly valid under conditions of short residence time and rapid gas expansion. Therefore, the temperature T_{mix} should be interpreted

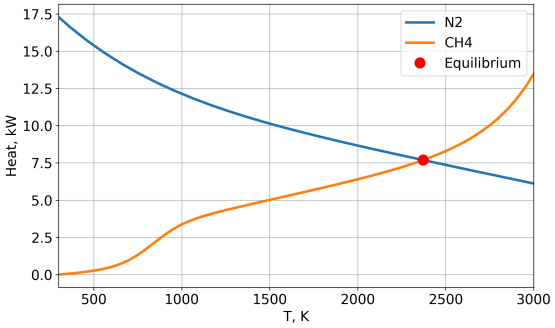

Figure 5. Heat content variation of the N_2 plasma jet and the CH_4 stream.

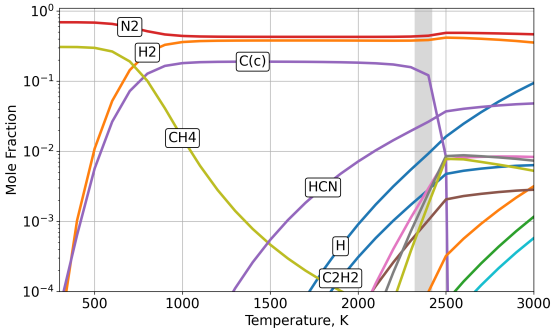

Figure 6. Calculated gas composition under thermodynamic equilibrium conditions.

as a representative average value rather than a physically resolved local temperature.

The outlet gas composition was further estimated using a thermodynamic equilibrium model assuming chemical freeze-out at the mixing temperature T_{mix}. According to the equilibrium calculations (Figure 6), the dominant species are N_2 (52 vol.%) and H_2 (33 vol.%), along with smaller fractions of HCN (2.7 vol.%) and atomic hydrogen (0.9 vol.%). However, these predictions do not fully agree with the experimental observations, which indicate the presence of residual hydrocarbons at approximately 4.3 vol.%. This discrepancy is attributed to the short residence time in the reforming zone, which prevents the completion of all chemical reactions and limits the establishment of thermodynamic equilibrium.

Solid carbon formation was observed in all experimental runs conducted in this study. The downstream gas-cleaning system, composed of a cyclone separator, a bag filter, and a gas scrubber, enabled the collection of carbonaceous material at all processing stages. Subsequent analysis confirmed the presence of solid carbon (carbon black/soot) produced during the plasma-assisted methane pyrolysis process.

It should be emphasized that the equilibrium calculations do not describe the detailed quenching chemistry occurring during the post-plasma cooling process and therefore should be interpreted only as a first-order thermodynamic estimate of the final gas composition. In particular, finite-rate chemical kinetics during rapid cooling may substantially modify the concentrations of reactive intermediate species predicted under equilibrium conditions. Consequently, a kinetic modeling approach is required to accurately describe the gas-phase composition under the investigated operating conditions.

Consequently, a kinetic modeling approach is required to accurately describe the gas-phase composition under the investigated operating conditions, where non-equilibrium effects and kinetically limited reactions play a dominant role. A more detailed thermo-fluid model including spatially resolved temperature fields is the subject of ongoing work.

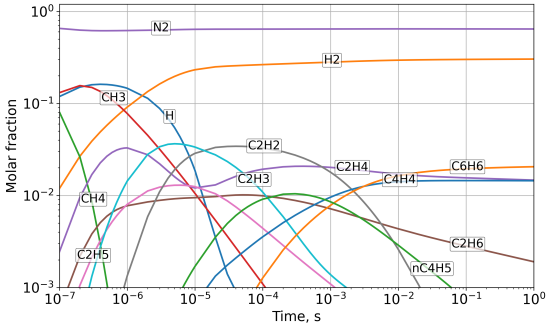

Figure 7. Temporal evolution of molar fractions of chemical species during methane pyrolysis at 2370 K predicted by the gas-phase kinetic model.

Figure 7 shows the temporal evolution of the molar fractions of the chemical species involved in methane pyrolysis at a fixed temperature of 2370 K, as predicted by the gas-phase kinetic model. Time is represented on a logarithmic scale ranging from 10^{-7} to 1 s, while the molar fractions are also displayed on a logarithmic scale to capture the wide dynamic range of species concentrations.

Nitrogen, used as the plasma-forming and carrier gas, exhibits an essentially constant molar fraction throughout the entire time interval, indicating its inert behavior within the considered kinetic mechanism. In contrast, molecular hydrogen shows a continuous increase in molar fraction, becoming one of the dominant species at longer residence times, consistent with the progressive decomposition of methane and subsequent hydrogen recombination reactions.

Methane is rapidly consumed during the initial stages of the process, with a sharp decrease in its molar fraction occurring within the first microseconds. Short-lived radical species such as H, CH_3, and CH_2, exhibit pronounced transient maxima at early times, reflecting their role as primary intermediates in the methane dissociation pathways. These radicals are subsequently consumed through recombination and chain-propagation reactions, leading to the formation of larger hydrocarbon species.

The model predicts the formation of C_2 hydro-

Species	10^{-5}	10^{-3}	10^{-2}	10^{-1}	1
C_2H_2	0.0287	0.0179	0.0026	–	–
C_2H_3	0.0336	0.0014	–	–	–
C_2H_4	0.0121	0.0202	0.0171	0.0156	0.0147
C_2H_5	0.0125	0.0011	–	–	–
C_2H_6	0.0095	0.0072	0.0043	0.0028	0.0019
C_4H_4	–	0.0096	0.0141	0.0145	0.0145
C_6H_6	–	0.0078	0.0164	0.0195	0.0205
CH_3	0.0105	–	–	–	–
H	0.0187	–	–	–	–
H_2	0.2325	0.2812	0.2955	0.3011	0.3037
N_2	0.6394	0.6450	0.6465	0.6456	0.6446
nC_4H_5	0.0017	0.0085	0.0029	–	–
$\Sigma\ C_xH_y$	0.1086	0.0737	0.0574	0.0524	0.0516

Table 1. Gas composition as a function of time during methane pyrolysis.

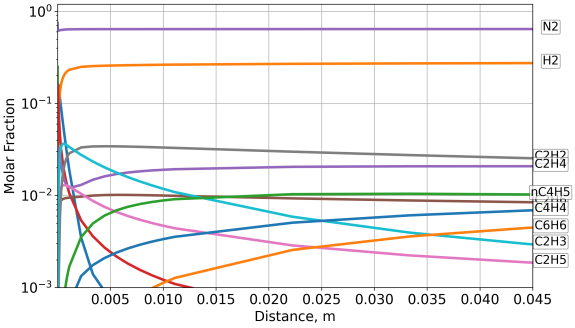

Figure 8. Numerical prediction of axial evolution of gas-phase molar fractions under isothermal conditions at 2370 K.

carbons (C_2H_2, C_2H_3, and C_2H_4) at intermediate times, followed by their gradual consumption as heavier hydrocarbons are formed. At longer times, species with higher molecular weight, such as C_4H_4, nC_4H_5, and C_6H_6, become noticeable, indicating the onset of molecular growth processes and the formation of aromatic precursors associated with carbon nucleation. Gas-phase compositions for various residence times are detailed in Table 1 .

For times exceeding 2×10^{-2} s the sum of the molar fractions of the dominant species remains nearly constant, suggesting that the system approaches a quasi-steady state under the imposed conditions. The last row of Table 1 summarizes the molar fractions of species with values higher than 0.001. For times above 10^{-2} s the total molar fraction of hydrocarbons gradually decreases and stabilizes in the range of 5–6 vol.%. This level is of the same order of magnitude as the experimental measurements, which indicate approximately 4 vol.% of CxHy species at the reactor outlet, although quantitative differences are expected due to kinetic limitations and finite residence times.

Figure 8 illustrates the spatial evolution of the molar fractions of the chemical species along the reactor axis at a fixed temperature of 2370 K. In this representation, the independent variable corresponds to the axial distance measured from the methane injection location, obtained by mapping the temporal solution of the kinetic model onto the spatial coordinate using the local axial velocity. The calculated profiles show a rapid consumption of methane in the vicinity of the injection point, followed by the progressive establishment of a composition dominated by stable species. Reactive radicals and short-lived intermediates are confined to a narrow upstream region, whereas downstream the molar fractions of the main species vary smoothly along the channel. Nitrogen remains the major component throughout the domain, acting as an inert carrier gas, while hydrogen and C_2 hydrocarbons reach quasi-constant levels over most of the reactor length. These axial profiles provide the basis for coupling the kinetic model with the reactor geometry and residence-time distribution adopted in the simulations.

The predicted molar fraction of hydrogen reaches approximately 30 vol%, which is of the same order of magnitude as the experimental value of 21 vol%. The remaining discrepancy can be attributed to the simplifying assumptions adopted in the model, including the use of a reduced gas-phase reaction mechanism, the assumption of spatially uniform temperature, and the neglect of heat losses and incomplete quenching effects. In addition, the short residence time and the strong turbulence in the plasma–methane interaction region may limit the extent of hydrogen formation under experimental conditions, leading to lower measured concentrations compared to the idealized numerical predictions.

The high nitrogen content in the outlet stream, resulting from the use of N_2 both as the plasma-forming gas and as the quenching medium, leads to significant dilution of the produced hydrogen. Therefore, direct utilization of the generated gas for applications requiring high-purity hydrogen would require an additional H_2/N_2 separation step. On the other hand, for large-scale hydrogen production, the resulting H_2–N_2 mixture may also represent a potentially useful intermediate stream, since the presence of hydrogen provides elevated heating value, while nitrogen contributes to stable plasma operation in subsequent high-power plasma processes. Future work will focus on more detailed experimental characterization, including spatially resolved measurements and advanced thermo-fluid modeling, to improve understanding of the coupled transport and reaction phenomena governing plasma-assisted methane pyrolysis.

4. Conclusions

Methane pyrolysis assisted by a DC thermal plasma jet was investigated experimentally and through thermodynamic and kinetic modeling approaches. Stable operation of the plasma torch was achieved by in-

jecting methane into the post-discharge region of the nitrogen plasma jet, avoiding direct interaction with the arc column and reducing operational instabilities associated with carbon deposition and arc fluctuations.

Under steady-state operating conditions (150 A, 250 V, 90 slpm of N_2 and 40 slpm of CH_4), experimental measurements showed that the reactor produced an outlet gas containing approximately 20.9 vol% H_2 and 4.3 vol% residual hydrocarbons (reported as CH_4-equivalent), corresponding to an experimentally estimated methane conversion of approximately 92 %. Solid carbon formation was observed in all experiments, confirming the occurrence of methane pyrolysis under the investigated conditions.

Thermodynamic equilibrium calculations predicted hydrogen-rich gas compositions at elevated temperatures, with equilibrium H_2 fractions approaching 30 vol%. However, significant discrepancies between equilibrium predictions and experimental measurements demonstrated that the process operates under kinetically controlled non-equilibrium conditions. In particular, finite residence times, rapid quenching, and strong temperature gradients limit the completion of chemical reactions and promote the persistence of residual hydrocarbons in the outlet gas.

The kinetic model successfully reproduced the main experimental trends and provided insight into the temporal and spatial evolution of the reacting system. Model predictions revealed rapid methane dissociation in the initial stages of the process, followed by the formation of short-lived radicals and intermediate hydrocarbons prior to the establishment of quasi-steady gas compositions. The predicted hydrogen mole fraction was of the same order of magnitude as the experimental measurements, supporting the applicability of the proposed thermodynamic–kinetic modeling framework.

Overall, the results demonstrate that post-discharge plasma-assisted methane pyrolysis is a viable route for turquoise hydrogen production and highlight the importance of non-equilibrium kinetic effects in determining the final gas composition under thermal plasma conditions.

This article was edited with the assistance of ChatGPT (OpenAI), used for improving English grammar and style. All scientific interpretations and conclusions are solely the responsibility of the authors.

Acknowledgements

This work was supported by the São Paulo Research Foundation (FAPESP) under Grant No. 2022/00271-3.

The authors acknowledge the Plasma and Process Laboratory and the Eneva H_2 Turquoise Project for providing experimental infrastructure and technical support throughout this research.

References

[1] J. Osorio-Tejada, K. Van'T Veer, N. V. D. Long, et al. Sustainability analysis of methane-to-hydrogen-to-ammonia conversion by integration of high-temperature plasma and non-thermal plasma processes. *Energy Conversion and Management*, 269:116095, 2022-10. doi:10.1016/j.enconman.2022.116095.

[2] E. Dames, V. Rohani, and L. Fulcheri. Plasma chemistry and plasma reactors for turquoise hydrogen and carbon nanomaterials production. In *Advances in Chemical Engineering*, volume 61, pages 253–317. Elsevier, 2023. ISBN 978-0-323-95774-8. doi:10.1016/bs.ache.2023.05.001.

[3] A. Fridman. Plasma chemistry: Plasma-chemical fuel conversion and hydrogen production, 2008. Pages: 676-754. doi:10.1017/CBO9780511546075.012.

[4] A. Essiptchouk, F. Miranda, and G. Petraconi. Comparative analysis of methane conversion: pyrolysis, dry and steam thermal plasma reforming. *Journal of Physics D: Applied Physics*, 57(24):245201, 2024-06-14. doi:10.1088/1361-6463/ad31e7.

[5] J. R. Fincke, R. P. Anderson, T. A. Hyde, and B. A. Detering. Plasma pyrolysis of methane to hydrogen and carbon black. *Industrial & Engineering Chemistry Research*, 41(6):1425–1435, 2002-03-01. doi:10.1021/ie010722e.

[6] L. Fulcheri. From methane to hydrogen, carbon black and water. *International Journal of Hydrogen Energy*, 20(3):197–202, 1995-03. doi:10.1016/0360-3199(94)E0022-Q.

[7] L. Fulcheri. Direct decarbonization of methane by thermal plasma for the co production of hydrogen and carbon nanostructure, 2018.

[8] M. Gautier, V. Rohani, and L. Fulcheri. Direct decarbonization of methane by thermal plasma for the production of hydrogen and high value-added carbon black. *International Journal of Hydrogen Energy*, 42(47):28140–28156, 2017-11. doi:10.1016/j.ijhydene.2017.09.021.

[9] M. Hrabovsky, M. Hlina, V. Kopecky, et al. Steam plasma methane reforming for hydrogen production. *Plasma Chemistry and Plasma Processing*, 38(4):743–758, 2018-07. doi:10.1007/s11090-018-9891-5.

[10] A. Tamošiūnas, P. Valatkevičius, D. Gimžauskaitė, et al. Glycerol steam reforming for hydrogen and synthesis gas production. *International Journal of Hydrogen Energy*, 42(17):12896–12904, 2017-04. doi:10.1016/j.ijhydene.2016.12.071.

[11] H.-Y. Lian, X.-S. Li, J.-L. Liu, and A.-M. Zhu. Methanol steam reforming by heat-insulated warm plasma catalysis for efficient hydrogen production. *Catalysis Today*, 337:76–82, 2019-10. doi:10.1016/j.cattod.2019.03.068.

[12] G. P. e. a. Smith. Gri-mech 3.0. http://combustion.berkeley.edu/gri-mech/, 2000.